2018 IEEE Intelligent Vehicles Symposium (IV)
Changshu, Suzhou, China, June 26-30, 2018

Vehicle Localization using 76GHz Omnidirectional Millimeter-Wave Radar for Winter Automated Driving*

Keisuke Yoneda[1], Naoya Hashimoto[1], Ryo Yanase[1], Mohammad Aldibaja[1] and Naoki Suganuma[1]

Abstract— **This paper presents the 76GHz MWR (Millimeter-Wave Radar)-based self-localization method for automated driving during snowfall. Previously, there were many LIDAR (Light Detection and Ranging)-based localization techniques proposed for high measurement accuracy and robustness to changes of day and night. However, they did not provide effective approaches for snow conditions because of sensing noise (i.e., environmental resistance) created by snowfall. Therefore, this paper developed a MWR-based map generation and a real-time localization method by modeling the uncertainties of error propagation. Quantitative evaluations are performed on driving data with and without snow conditions, using a LIDAR-based method as the baseline. Experimental results show that a lateral root mean square error of about 0.25m can be obtained, regardless of the presence or absence of snowfall. Thus, it can be investigated that a potential performance of radar-based localization.**

I. Introduction

Automated vehicle technology has reached the era of comprehensive testing and practical applications. Many automotive companies and research organizations have conducted driving experiments on public roads [1], [2]. Such vehicles are equipped with various sensors including LIDAR (Light Detection and Ranging), MWR (Millimeter-Wave Radar), the camera and GNSS/IMU (Global Navigation Satellite System /Inertial Measurement Unit) system to percept surroundings and allow autonomous behavior. These sensor data are used to attain the following objectives.

- Environmental perception: detect static/dynamic object and dynamic road object (e.g., traffic signal status).
- Self-localization: estimate own position on a precise digital map.
- Motion planning: generate safety trajectory, considering traffic rules.
- Motion control: determine adequate control signals for steering, acceleration, and braking.

In order to achieve safe driving on a public road, a common approach is implementing robust perception and decision-making systems using precise digital maps. For example, by referring to the map relating to traffic light position, it is possible to accurately and quickly recognize the state of the traffic light [3], [4]. To smoothly control the vehicle by referring to the map according to the estimated position, decimeter-level positional accuracy is required. The general strategy of self-localization is map-matching using a precisely predefined map.

LIDAR-based methods have been proposed because of their high measurement accuracy and robustness to changes in day and night. In [5], a method was proposed in which a map was created by mapping the infrared reflectivity of the road surface. The vehicle position was then estimated as a probability distribution by applying template-matching between the map and the real-time LIDAR point cloud. This approach was implemented on road-paint information, and reported positional accuracy at the decimeter-level. However the problem with the LIDAR-based method is the bad weather, such as rain and snowfall. For example, during snowfall, landmarks cannot be observed because the road surface is occluded. In order to resolve such difficulties, an algorithm for reconstructing observation information of LIDAR was proposed for the situation in which the road surface is partially occluded [6]. However, it can not be applied to situations where the road surface is completely occluded. Methods have also been proposed that exploit the features of the surrounding buildings by utilizing the 3-D point cloud map [7], [8]. However, because the shape of the roadside changes during snowfall, it is not an effective approach for snow conditions. Therefore, MWR can be used as a sensor to robustly observe surrounding objects during snowfall.

MWR is excellent for penetrating environmental resistance. However, it has the disadvantage of sparse observation information, owing to the low resolution of the angular direction compared to LIDAR. In previous studies, the self-localization methods were proposed to utilize MWR [9], [10]. In [9], a map generation method was proposed that clustered radar observations. Vehicle position was estimated using a particle filter. However, sufficient positioning accuracy was not obtained for self-driving because the obtained accuracy was the meter-level. In [10], a method using MWR and images from the around view monitor (AVM) was proposed. Road-level localization was implemented using MWR and then the accurate vehicle position is estimated using the AVM image by matching lane boundaries as a lane-level localization. Even with this method, it was assumed that sufficient precision could not be obtained with only MWR. Furthermore, the lane-level localization could not be utilized when lane boundaries were occluded by snow. Therefore, this study proposes a self-localization method using 76GHz MWR observation, measuring the performance in snow conditions and comparing with the LIDAR-based approach. The evaluation is performed using a high-precision

*This work was supported by Kanazawa University

[1]K. Yoneda, N. Hashimoto, R. Yanase, M. Aldibja and N. Suganuma are with Kanazawa University, Kakuma-cho, Kanazawa, Ishikawa, 920-1192, Japan.
k.yoneda@staff.kanazawa-u.ac.jp

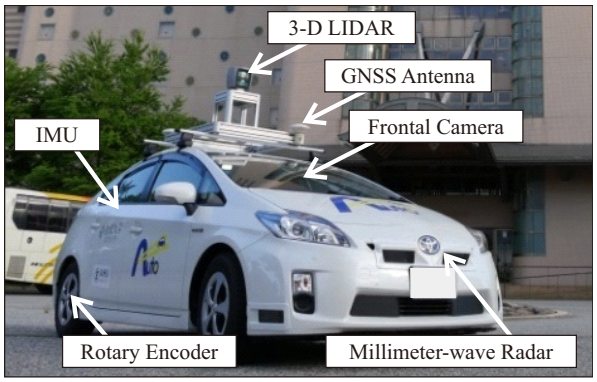

(a) Experimental Vehicle

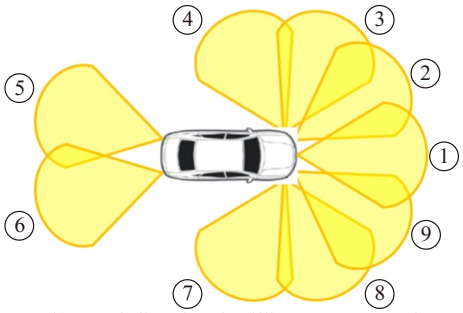

(b) Omni-directional Millimeter-wave Radar

Fig. 1. Experimental Vehicle

RTK-GNSS (Real Time Kinematic GNSS) with a post-processing, providing centimeter positional accuracy. The key contributions of this paper are as follows.

- Development of both map generation and localization by modeling uncertainties of MWR, based on error propagation.
- Quantitative evaluations for accuracy of self-localization against snowfall, comparing with LIDAR-based method as baseline.

The rest of this paper is composed as follows. Section II introduces the experimental vehicle. Section III explains the 2-D map generation using MWR. The proposed localization method is detailed in Section IV. Section V describes numerical experiments for urban driving data and evaluation results. Finally, Section VI concludes with the obtained results and offers directions for future work.

II. Experimental Vehicle

Figure 1(a) illustrates our experimental vehicle. The vehicle is equipped with an Applanix POS/LV220 coupled GNSS and IMU system. It provides position (i.e., latitude, longitude and altitude) and orientation (pitch, yaw, roll) at 100Hz. A 3-D LIDAR Velodyne HDL-64E S2 with 64 separate beams is mounted on a vehicle to take measurements of the environment. It measures 3-D omnidirectional distance under a frequency of about 10Hz. Nine MWRs are installed inside the front and rear bumpers to recognize distant objects, as shown in Fig. 1(b). It measures distance, angle and relative velocity for objects at 20Hz. The horizontal field-of-view is 40deg. The number of observations for each MWR is 40.

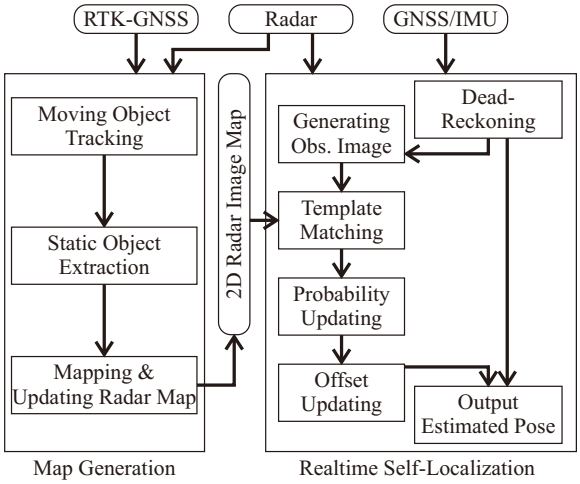

Fig. 2. Proposed Localization Method

III. Map Generation

A. Method

A reference map is generated by mapping MWR observations using the RTK-GNSS with post-processing. The measuring angle sensing accuracy of 76GHz MWR is generally not precise compared to LIDAR and 79GHz MWR. Therefore, it is necessary to consider measurement accuracy during the mapping procedure. According to the left-side of Fig. 2, the reference map is generated using the following processes.

1) Object tracking: estimate static/dynamic bbjects.
2) Static object extraction: remove dynamic objects.
3) Mapping: update a probability of the static objects in each map pixel.

B. Object Tracking

Object tracking estimates static/dynamic objects using MWR observations. The interactive multiple model (IMM) [11] is adopted to integrate multiple types of motions to estimate position, velocity, and acceleration for the object. Constant acceleration, constant velocity, and stop models are defined as motion models. The state variable, $\boldsymbol{x}^{mwr}$ is defined in Eq. (1).

$$\boldsymbol{x}^{mwr} = [p^x, p^y, v^x, v^y, a^x, a^y]^T \tag{1}$$

$$\boldsymbol{w}^{mwr} = [w^{p^x}, w^{p^y}, w^{\dot{a}^x}, w^{\dot{a}^y}]^T \tag{2}$$

where, p^x and p^y are object position in global coordinates of the Universal Transverse Mercator (UTM) [12]. v^x, a^x, v^y, and a^y are velocity and acceleration for the x and y coordinates, respectively. w^{mwr} is a process noise vector for corresponding variables. For example, a state equation of the independent constant acceleration model can be formulated

as the follows.

$$\begin{aligned}\boldsymbol{x}_t^{mwr} &= F\boldsymbol{x}_{t-\Delta t}^{mwr} + G\boldsymbol{w}_t^{mwr} \\ &= \begin{bmatrix} 1 & 0 & \Delta t & 0 & \Delta t^2/2 & 0 \\ 0 & 1 & 0 & \Delta t & 0 & \Delta t^2/2 \\ 0 & 0 & 1 & 0 & \Delta t & 0 \\ 0 & 0 & 0 & 1 & 0 & \Delta t \\ 0 & 0 & 0 & 0 & 1 & 0 \\ 0 & 0 & 0 & 0 & 0 & 1 \end{bmatrix} \boldsymbol{x}_{t-\Delta t}^{mwr} \\ &+ \begin{bmatrix} \Delta t & 0 & 0 & 0 \\ 0 & \Delta t & 0 & 0 \\ 0 & 0 & \Delta t^2/2 & 0 \\ 0 & 0 & 0 & \Delta t^2/2 \\ 0 & 0 & \Delta t & 0 \\ 0 & 0 & 0 & \Delta t \end{bmatrix} \boldsymbol{w}_t^{mwr} \end{aligned} \tag{3}$$

In the case of the constant velocity model, the acceleration values are set to zero. Similarly, in the case of the stop model, the velocity and accelerations are set to zero. Additionally, models having a constant yaw rate are defined to express vehicle motion with nonholonomic system. The IMM can track surrounding dynamic objects, such as vehicles and bicycles. Therefore, dynamic objects can be ignored for map generation.

C. Mapping

The reference map is generated using static objects which obtained by remove those dynamic objects. Observation points in the global coordinates are transformed into 2-D image coordinates and mapped to corresponding pixels. In order to consider the low sensing accuracy of MWR, the existence likelihood is defined using a covariance matrix P, based on observational error propagation, as described in the Appendix. Figure 3(a) indicates an example of mapping process. The existence likelihood is computed to produce a variance perpendicular to the irradiation direction of the sensor. A likelihood value for each pixel is obtained via integration in the corresponding area of the likelihood distribution. The existence probability is then updated, based on the likelihood value. Figure 3(b) shows the obtained image map. Each pixel has information about latitude and longitude. By comparing with the LIDAR-based map, as shown in Fig. 3(c), the obtained map includes objects on the sidewalk, such as telegraph poles and guardrails.

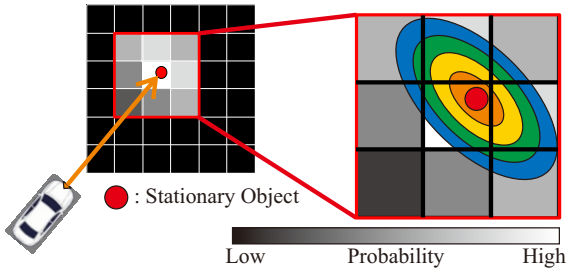

(a) Mapping MWR Observation

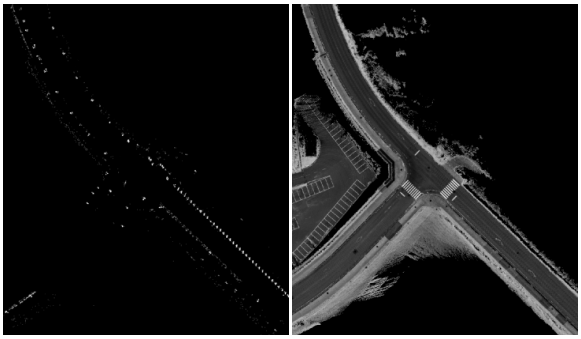

(b) MWR Image Map (c) LIDAR Image Map

Fig. 3. Map Generation

IV. Self-Localization

A. Method

In order to estimate vehicle position, our proposed method utilizes dead-reckoning to update the estimated position. Dead-reckoning updates position $[x_{d,t}, y_{d,t}]^T$ by time integration of linear velocity and yaw rate. However, it has the potential problem of accumulating positioning errors owing to sensing accuracy. The proposed method then estimates the error (offset) $[\Delta x_{d,t}, \Delta y_{d,t}]^T$ of the dead-reckoning by matching the observation to the MWR map, as shown in the right side of Fig. 2. The vehicle position x_t, y_t is expressed in the following equation.

$$[x_t, y_t]^T = [x_{d,t}, y_{d,t}]^T + [\Delta x_{d,t}, \Delta y_{d,t}]^T \tag{4}$$

The offset $[\Delta x_{d,t}, \Delta y_{d,t}]^T$ is estimated with the following procedures.

1) Obtain an observation image by the same procedure as the map generation using MWR data of the latest N frames.
2) Search surrounding MWR image map as the map image.
3) Estimate probability P_t of the positioning offset by map-matching.
4) Update the offset values $[\Delta x_{d,t}, \Delta y_{d,t}]^T$ based on the yielded probabilities P_t.

Orientation values generally are estimated with a positioning offset. For simplicity, this study only estimates the positioning offset $[\Delta x_{d,t}, \Delta y_{d,t}]^T$. The orientation is directly given from the GNSS/IMU sensor.

B. Observation Image Generation and Map Extraction

Observation image and map images are prepared to apply map-matching. Like the map generation in the previous section, stationary objects obtained from MWR are mapped to create the observation image in the North-East (NE) coordinates. Figure 4(b) is an observation image in a typical driving scene. The center of the image represents the current vehicle position. The observation image covers an area of 24m x24m. It is generated using multiple frames of observations, so that the observation point covers the whole region. The surrounding image map is extracted from the generated MWR map in the NE coordinates as well as the observation as shown in Fig. 4(c). The map image covers an area of 32m x32m.

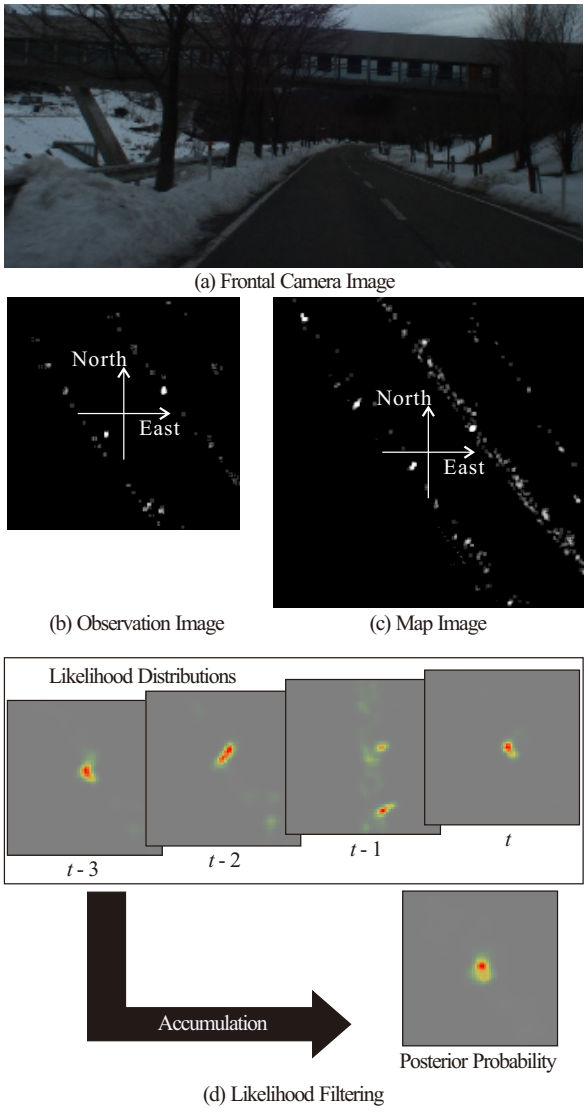

(a) Frontal Camera Image

(b) Observation Image (c) Map Image

(d) Likelihood Filtering

Fig. 4. Map Matching

C. Image Correlation

Image template-matching is applied to obtain a correlation distribution around the current position. Zero-means normalized cross-correlation (ZNCC) $R_{t,Ref}(\boldsymbol{\Delta x})$ is introduced as a cost function for template-matching.

$$R_{t,Ref}(\boldsymbol{\Delta x}) = \frac{\sum_{i,j}(m_{i,j}(\boldsymbol{\Delta x}) - \bar{m}(\boldsymbol{\Delta x}))(z_{i,j} - \bar{z})}{\sqrt{\sum_{i,j}(m_{i,j}(\boldsymbol{\Delta x}) - \bar{m}(\boldsymbol{\Delta x}))^2 \sum_{i,j}(z_{i,j} - \bar{z})^2}} \quad (5)$$

where, $R_{t,Ref}(\boldsymbol{\Delta x})$ is a ZNCC feature at a positioning offset $\boldsymbol{\Delta x} = [\Delta x, \Delta y]^T$. $\boldsymbol{z}$ and $\boldsymbol{m}$ are the observation and the map image, respectively. $\bar{z}$ is an average pixel value for the observation image. $\bar{m}(\boldsymbol{\Delta x})$ is an average pixel value for the corresponding region of the map image at $\boldsymbol{\Delta x}$.

However, it is difficult to obtain a high correlation value from ZNCC because observation points are sparse. Thus, the result of the correlation distribution in each frame cannot be reliable. Therefore, gamma correction is applied to preempt excessive responses for the probability.

$$R_t(\boldsymbol{\Delta x}) = \max(R_{t,Ref}(\boldsymbol{\Delta x}), 0.0)^{\gamma} \quad (6)$$

where γ is a gamma value for gamma correction. $R_t(\boldsymbol{\Delta x})$ is a likelihood distribution at $\boldsymbol{\Delta x}$.

D. Probability and Offset Updating

The probability distribution $P(\boldsymbol{\Delta x})$ of the positioning offset $[\Delta x_{d,t}, \Delta y_{d,t}]^T$ is updated using the likelihood distribution. As shown in Fig. 4(d), the likelihood distribution obtained in each frame is unstable. Although there are some frames that give clear peaks, they may suddenly show different distributions. Therefore, the accumulative distribution $P_t(\boldsymbol{\Delta x})$ is calculated by the cumulative processing of the likelihood distribution. Then, the probability distribution$P(\boldsymbol{\Delta x})$ is obtained by normalizing $P_t(\boldsymbol{\Delta x})$.

$$P_t(\boldsymbol{\Delta x}) = \beta P_t(\boldsymbol{\Delta x}) + R_n(\boldsymbol{\Delta x}) \quad (7)$$

$$P(\boldsymbol{\Delta x}) = P_t(\boldsymbol{\Delta x}) / \max(P_t) \quad (8)$$

where β is the decay rate for the accumulation process ($0 \leq \beta \leq 1$). Finally, the positioning offset value is estimated using weighted average values of the obtained probability.

$$\Delta x_{d,t} = \Delta x_{d,t-1} + g_{pos} \frac{\sum_{\boldsymbol{\Delta x}}(P(\boldsymbol{\Delta x})\Delta x)}{\sum_{\boldsymbol{\Delta x}} P(\boldsymbol{\Delta x})} \quad (9)$$

$$\Delta y_{d,t} = \Delta y_{d,t-1} + g_{pos} \frac{\sum_{\boldsymbol{\Delta x}}(P(\boldsymbol{\Delta x})\Delta y)}{\sum_{\boldsymbol{\Delta x}} P(\boldsymbol{\Delta x})} \quad (10)$$

where, g_{pos} is the gain value of offset-updating ($0 \leq g_{pos} \leq 1$).

V. Evaluation

A. Conditions

In order to evaluate the performance of the proposed method, experiments were carried out with driving data. Longitudinal and lateral errors were calculated between the obtained position and the ground-truth position. The GNSS was used to initialization of the original location. The RTK-GNSS was used as the ground-truth for evaluating the accuracy of the obtained position. The proposed method was compared with the LIDAR-based method as baseline method which is described in [13]. It estimate the position by matching features of road paint. The main difference between the proposed method and the baseline method is the sensor (i.e., MWR or LIDAR) and the image map (i.e., MWR map or LIDAR map). The baseline method estimates the offset value by map-matching for laser refrectivities for road surface.

The following evaluations are performed using two kinds of traveling areas.

- Evaluate positioning accuracy for summer driving data using the short course as shown in Fig. 5.
- Evaluate positioning accuracy for partially snowy driving data with using the short course.
- Evaluate positioning accuracy for fully snowy driving data with using the long course as shown in Fig. 6.

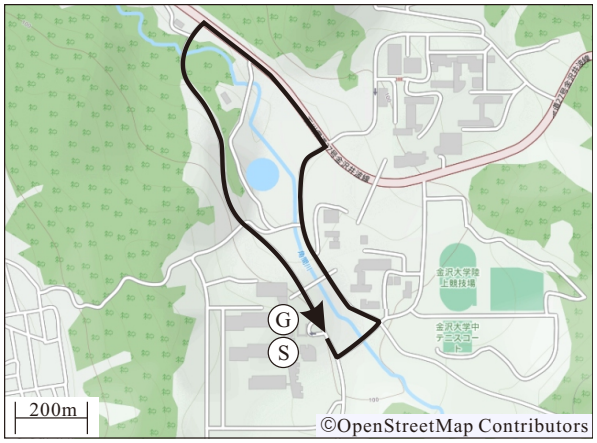

Fig. 5. Short Driving Route in Kanazawa-City

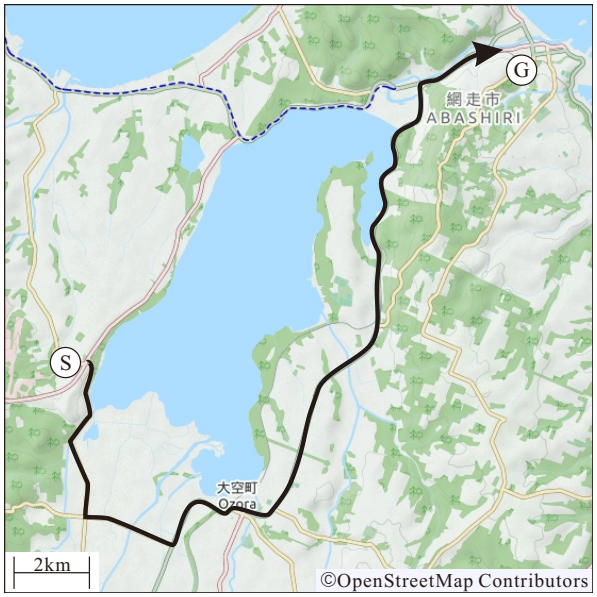

Fig. 6. Long Driving Route in Abashiri-City

The driving data was recorded on a public road by manual driving. In the short course, the total length of the route is about 2.15km in Kanazawa-city, Japan. We recorded the data during summer and winter seasons to evaluate the performance for the proposed method and the baseline method under snowy conditions. In the winter data, the sidewalk was covered with snow as shown in Fig. 4(a). In the long course, the winter driving data was recorded on a public road in Abashiri-city, Japan. The total length of the route is about 25km. In this data, the proposed method was only evaluated because the road surface was fully covered by snow.

B. Results

The experimental results in Table I show longitudinal and lateral root mean square (RMS) errors for conditions with and without snow. Both methods show reasonable positional accuracy in the case without snow. However, the proposed method showed the same degree of accuracy with snow, but the error of the baseline method deteriorated.

TABLE I
ROOT MEAN SQUARE ERRORS

	RMS Error	
	Longitudinal Error [m]	Lateral Error [m]
w/o Snow Condition		
Proposed Method	0.187	0.255
Baseline Method	0.253	0.159
w/ Snow Condition (Partially Covered)		
Proposed Method	0.223	0.232
Baseline Method	2.791	2.661
w/ Snow Condition (Fully Covered)		
Proposed Method	0.534	0.248

Figure 7 and Figure 8 show longitudinal, lateral errors and yaw rate for the proposed and the baseline methods with and without snow for the short course. During non-snowfall, errors within 1m were maintained for both methods, regardless of intersections and straight roads, as shown in Fig. 7. However, with the baseline method during snowfall, the lateral error immediately increased to 2m or more and the error could not be corrected thereafter, as shown in Fig. 8. Because snow-covered areas beside the road were observed as regions having high reflectivity by LIDAR, misalignment in the lateral direction occurred because of confusion with lane-road markings. Under this bad weather condition, the proposed method had the same tendency error as non-snowfall by using MWR, which is robust to snow conditions. Although the observation accuracy of MWR is not high compared with LIDAR, the proposed method shows the robustness against snowfall.

Figure 9 show longitudinal, lateral errors and yaw rate for the proposed method with and without snow for the long course. It can be confirmed that the proposed method maintained the same lateral accuracy regardless of the amount of snowfall. However, the longitudinal accuracy was deteriorated more than twice as compared with the result at the non-snowfall. Table II indicates the average number of observation points used for an observation image of a single frame. It was confirmed that appropriate matching result could not be obtained because the number of observation points became sparse. It is necessary to adjust so that the range of the observation image is adjusted to obtain sufficient matching result. From the above experimental results, the effectiveness of the proposed self-localization was confirmed in snow conditions.

VI. CONCLUSION

The self-localization method was proposed using 76GHz MWR. Experimental results show that an lateral RMS error of about 0.25m could be obtained, regardless of the presence or absence of snowfall. Although the obtained position accuracy was still not accurate enough for self-driving, it was possible to ensure safety by using it together with the LIDAR-based method. For example, in the scene where there was sudden snowfall after passing through a tunnel, the proposed method can be expected to estimate a position until the vehicle arrives autonomously to a safe area. In the future,

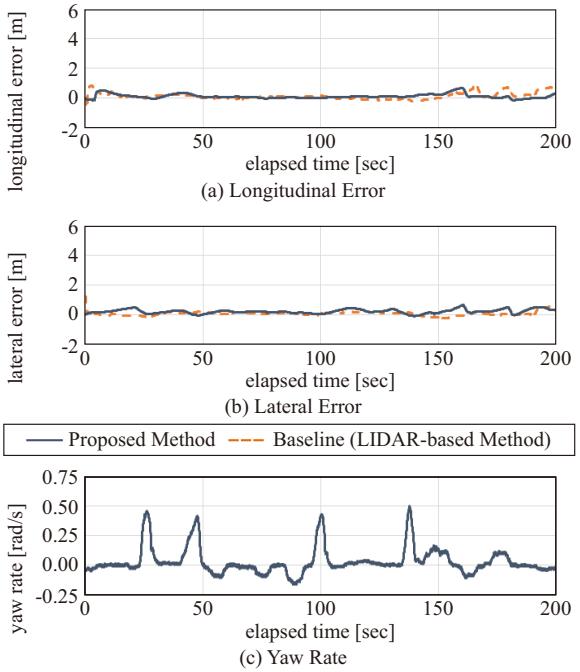

Fig. 7. Evaluated Results without Snow Condition for Short Course

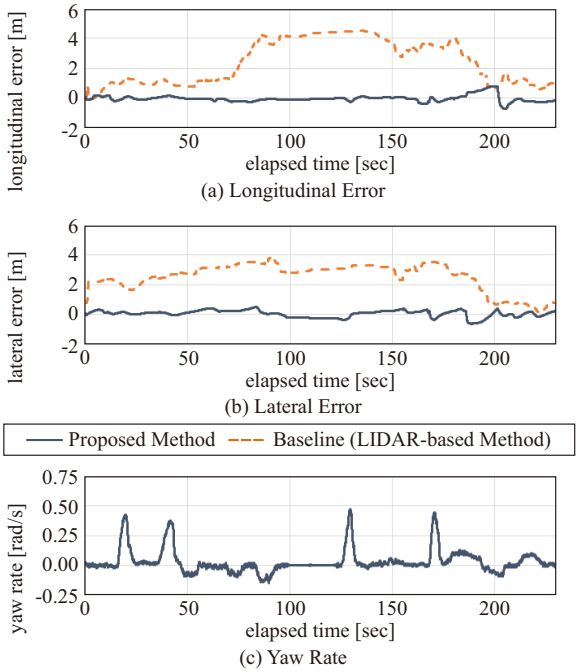

Fig. 8. Evaluated Results with Snow Condition (Partically Covered) for Short Course

stabilization and further improvements to the positioning accuracy can be obtained by acquiring more high-resolution data using 79GHz MWR.

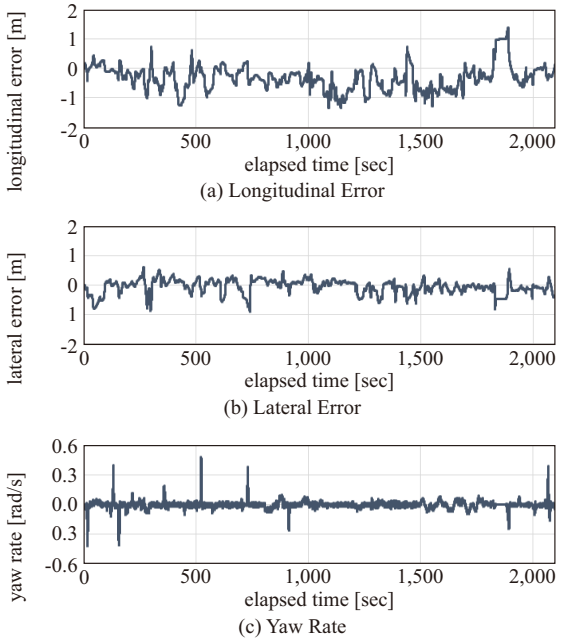

Fig. 9. Evaluated Results with Snow Condition (Fully Covered) for Long Course

TABLE II
AVERAGE NUMBER OF OBSERVATIONS USED FOR THE OBSERVATION IMAGE OF SINGLE-FRAME

Condition	Average Number of Observations
w/o Snow	156.855
w/ Snow (Partially Covered)	148.649
w/ Snow (Fully Covered)	74.493

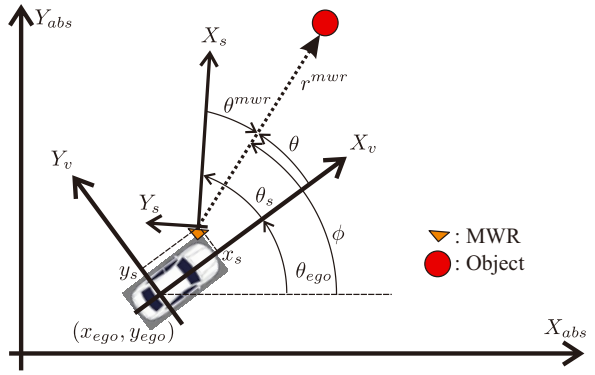

Fig. 10. Coordinate System

APPENDIX

OBSERVATION VALUE AND COVARIANCE MATRIX FOR MWR USING ERROR PROPAGATION

An observation value provided from MWR sensor data is represented as $\boldsymbol{z} = [x_g^{mwr}, y_g^{mwr}, v_{abs}^{mwr}]^T$. $[x_g^{mwr}, y_g^{mwr}]^T$ is the position of the observation in the global coordinates. v_{abs}^{mwr} is the absolute velocity in the MWR's irradiation direction. The MWR sensor data is a distance r^{mwr}, the irradiation direction θ^{mwr} and a relative velocity v^{mwr}in the irradiation direction. According to Fig. 10, the position of the

object can be transformed from the sensor coordinates to the global coordinates, as follows.

$$\begin{bmatrix} x^{mwr} \\ y^{mwr} \end{bmatrix} = \begin{bmatrix} r^{mwr}\cos\theta^{mwr} \\ r^{mwr}\sin\theta^{mwr} \end{bmatrix} \tag{11}$$

$$\begin{bmatrix} x_v^{mwr} \\ y_v^{mwr} \end{bmatrix} = \begin{bmatrix} \cos\theta_s & -\sin\theta_s \\ \sin\theta_s & \cos\theta_s \end{bmatrix} \begin{bmatrix} x^{mwr} \\ y^{mwr} \end{bmatrix} + \begin{bmatrix} x_s \\ y_s \end{bmatrix} \tag{12}$$

$$\begin{bmatrix} x_g^{mwr} \\ y_g^{mwr} \end{bmatrix} = \begin{bmatrix} \cos\theta_{ego} & -\sin\theta_{ego} \\ \sin\theta_{ego} & \cos\theta_{ego} \end{bmatrix} \begin{bmatrix} x_v^{mwr} \\ y_v^{mwr} \end{bmatrix} + \begin{bmatrix} x_{ego} \\ y_{ego} \end{bmatrix} \tag{13}$$

where, $[x^{mwr}, y^{mwr}]^T$ and $[x_v^{mwr}, y_v^{mwr}]$ are the object position in the sensor coordinates and the vehicle coordinates, respectively. $[x_s, y_s, \theta_s]^T$ is the sensor installation position in the vehicle coordinates. $[x_{ego}, y_{ego}, \theta_{ego}]$ is the vehicle position in the global coordinates.

The absolute velocity of the vehicle in the irradiation direction v_{ego}^{mwr} is calculated using vehicle velocity v_{ego}.

$$v_{ego}^{mwr} = v_{ego}\cos(\theta^{mwr} + \theta_s) \tag{14}$$

Thus, the observed value is expressed by the following equation.

$$\boldsymbol{z} = \begin{bmatrix} x_{ego} + x_s C_{ego} - y_s S_{ego} + r^{mwr} C_\phi \\ y_{ego} + y_s S_{ego} + y_s C_{ego} + r^{mwr} S_\phi \\ v_{ego}\cos\theta + v^{mwr} \end{bmatrix} \tag{15}$$

where $\phi = \theta_{ego} + \theta_s + \theta^{mwr}, \theta = \theta_s + \theta^{mwr}$. $S_{ego} = \sin\theta_{ego}, C_{ego} = \cos\theta_{ego}, S_\phi = \sin\phi, C_\phi = \cos\phi$. Therefore, the observation value $\boldsymbol{z}$ is expressed by the following function $\boldsymbol{h}$ having 10 variables.

$$\begin{aligned} \boldsymbol{z} = \boldsymbol{h}(&x_{ego}, y_{ego}, v_{ego}, \theta_{ego}, \\ &r^{mwr}, v^{mwr}, \theta^{mwr}, x_s, y_s, \theta_s) \end{aligned} \tag{16}$$

Based on the theory of error propagation, the error $\Delta\boldsymbol{z}$ of the observation $\boldsymbol{z}$ is approximated as the follows.

$$\begin{aligned} \Delta\boldsymbol{z} = &\frac{\partial \boldsymbol{h}}{\partial x_{ego}}\Delta x_{ego} + \frac{\partial \boldsymbol{h}}{\partial y_{ego}}\Delta y_{ego} + \frac{\partial \boldsymbol{h}}{\partial v_{ego}}\Delta v_{ego} + \\ &\frac{\partial \boldsymbol{h}}{\partial \theta_{ego}}\Delta\theta_{ego} + \frac{\partial \boldsymbol{h}}{\partial r^{mwr}}\Delta r^{mwr} + \frac{\partial \boldsymbol{h}}{\partial v^{mwr}}\Delta v^{mwr} + \\ &\frac{\partial \boldsymbol{h}}{\partial \theta^{mwr}}\Delta\theta^{mwr} + \frac{\partial \boldsymbol{h}}{\partial x^s}\Delta x^s + \frac{\partial \boldsymbol{h}}{\partial y^s}\Delta y^s + \frac{\partial \boldsymbol{h}}{\partial \theta^s}\Delta\theta^s \end{aligned} \tag{17}$$

Then, a covariance matrix P for the observation is obtained by solving the expected value of the squared error.

$$P = \begin{bmatrix} P_{11} & P_{12} & P_{13} \\ P_{21} & P_{22} & P_{23} \\ P_{31} & P_{32} & P_{33} \end{bmatrix} = E\left[\Delta z(\Delta z)^T\right] \tag{18}$$

$$\begin{aligned} P_{11} = &\sigma_{x_{ego}}^2 + \sigma_{\theta_{ego}}^2(r^{mwr}S_\phi + x_s S_{ego} + y_s C_{ego})^2 \\ &+ \sigma_{r^{mwr}}^2 C_\phi^2 + r^{mwr2} S_\phi^2 \sigma_\theta^2 + \sigma_{x_s}^2 C_{ego}^2 + \sigma_{y_s}^2 S_{ego}^2 \end{aligned} \tag{19}$$

$$\begin{aligned} P_{12} = P_{21} = &-(r^{mwr}S_\phi + x_s S_{ego} + y_s C_{ego}) \\ &(r^{mwr}C_\phi + x_s C_{ego} - y_s S_{ego}) + (\sigma_{x_s}^2 - \sigma_{y_s}^2) S_{ego} C_{ego} \\ &+ (\sigma_{r^{mwr}}^2 - r^{mwr2}\sigma_\theta^2) S_\phi C_\phi \end{aligned} \tag{20}$$

$$P_{13} = P_{31} = v_{ego} r^{mwr} \sigma_\theta^2 S_\phi \sin\theta \tag{21}$$

$$\begin{aligned} P_{22} = &\sigma_{y_{ego}}^2 + \sigma_{\theta_{ego}}^2(r^{mwr}C_\phi + x_s C_{ego} - y_s S_{ego})^2 \\ &+ \sigma_{r^{mwr}}^2 S_\phi^2 + r^{mwr2} C_\phi^2 \sigma_\theta^2 + \sigma_{x_s}^2 S_{ego}^2 + \sigma_{y_s}^2 C_{ego}^2 \end{aligned} \tag{22}$$

$$P_{23} = P_{32} = -v_{ego} r^{mwr} \sigma_\theta^2 C_\phi \sin\theta \tag{23}$$

$$P_{33} = \sigma_{v^{mwr}}^2(1 + \cos^2\theta) + v_{ego}^2 \sigma_\theta^2 \sin^2\theta \tag{24}$$

where $\sigma_\theta^2 = \sigma_{\theta^{mwr}}^2 + \sigma_{\theta_s}^2$. σ_* is a standard deviation for the corresponding variable.

ACKNOWLEDGMENT

This work was supported by a research grant from The Mazda Foundation.

REFERENCES

[1] U. Franke, D. Pfeiffer, C. Rabe, C. Knoeppel, M. Enzweiler, F. Stein and R. G. Herrtwich, "Making Bertha See", *ICCV Workshop on Computer Vision for Autonomous Driving*, 2013.

[2] S. Kato, E. Takeuchi, Y. Ishiguro, Y. Ninomiya, K. Takeda, and T. Hamada. "An Open Approach to Autonomous Vehicles", *IEEE Micro*, vol. 35, no. 6, pp. 60-69, 2015.

[3] N. Fairfield and C. Urmson, "Traffic Light Mapping and Detection", *Proceedings of the 2011 IEEE International Conference on Robotics and Automation*, pp. 5421-5426, 2011.

[4] K. Yoneda, N. Suganuma and M. Aldibaja, "Simultaneous Sate Recognition for Multiple Traffic Signals on Urban Road", *Proceedings of MECATRONICS-REM*, pp. 135-140, 2016.

[5] J. Levinson and S. Thrun, "Robust Vehicle Localization in Urban Environments Using Probabilistic Maps", *Proceedings of 2010 IEEE International Conference on Robotics and Automation*, pp. 4372-4378, 2010.

[6] M. Aldibaja, N. Suganuma and K. Yoneda, "Robust Intensity Based Localization Method for Autonomous Driving on Snow-wet Road Surface", *IEEE Transactions on Industrial Informatics*, vol. 13, no. 5, pp. 2369-2378, 2017.

[7] K. Yoneda, C. X. Yang, S. Mita, T. Okuya and K. Muto, "Urban Road Localization by using Multiple Layer Map Matching and Line Segment Matching", *Proceedings of 2015 IEEE Intelligent Vehicles Symposium*, pp.525-530, 2015.

[8] N. Akai, L. Y. Morales, E. Takeuchi, Y. Yoshihara, Y. Ninomiya, "Robust localization using 3D NDT scan matching with experimentally determined uncertainty and road marker matching", *Proceedings of 2017 IEEE Intelligent Vehicles Symposium*, pp. 1357-1364, 2017.

[9] F. Schuster, M. Wörner, C. G. Keller, M. Haueis andC. Curio, "Robust localization based on radar signal clustering", *Proceedings of 2016 IEEE Intelligent Vehicles Symposium*, pp. 839-844, 2016.

[10] S. Park, D. Kim and K. Yi, "Vehicle Localization using an AVM camera for An Automated Urban Driving", *Proceedings of 2016 IEEE Intelligent Vehicles Symposium*, pp. 871-876, 2016.

[11] R. Helmick, "IMM Estimator with Nearest-Neighbor Joint Probabilistic Data Association", *Multiagent-Multisensor Tracking: Applications and Advances Volume III*, Artech House Publishers, pp. 161-198, 2000.

[12] J. P. Snyder, "Map Projections: A Working Manual", Geological Survey(U.S.), 1987.

[13] N. Suganuma, D. Yamamoto and K. Yoneda, "Localization for Autonomous Driving on Urban Road", *Journal of Advanced Control, Automation and Robotics*, Vol. 1, No. 1, pp. 47-53, 2016.